XIV International Conference on Computational Plasticity. Fundamentals and Applications
COMPLAS 2017
E. Oñate, D.R.J. Owen, D. Peric and M. Chiumenti(Eds)

EXPERIMENTAL ANALYSIS AND NUMERICAL SIMULATION OF SINTERED MICRO-FLUIDIC DEVICES

M. SAHLI[*,†], J-C. GELIN[*] AND T. BARRIERE[*]

[*] FEMTO-ST Institute/Applied Mechanics Department, 24 chemin de l'épitaphe, 25000 Besançon, France
e-mail: tbarriere@femto-st.fr, jean-claude.gelin@univ-fcomte.fr

[†] Mechanics Laboratory, Faculty of Engineering Sciences, University Mentouri, 25000 Constantine, Algeria
email: sahlisofiane2@yahoo.fr

Key words: hot embossing, Sintering, Numerical simulation, Constitutive equations, 316L stainless steel powders.

Abstract. This paper investigates the use of numerical simulations to describe solid state diffusion of a sintering stage during a Powder Hot Embossing (PHE) process for micro-fluidic components. Finite element analysis based on a thermo-elasto-viscoplastic model was established to describe the densification process of a PHE stainless steel porous component during sintering. The corresponding parameters such as the bulk viscosity, shearing viscosity and sintering stress are identified from dilatometer experimental data. The numerical analyses, which were performed on a 3D micro-structured component, allowed comparison between the numerical predictions and experimental results of during a sintering stage. This comparison demonstrates that the FE simulation results are in better agreement with the experimental results at high temperatures.

1 INTRODUCTION

The metal hot embossing (MHE) process has become a viable, low cost process for producing parts with complex shapes in short series. MHE combines the shaping efficiency of polymer hot embossing with the capability of powder metallurgy [1-3], which offers many unique advantages in the production of near neat shape micro-structured components. This process is an actually a multi-step process divided into compounding, hot embossing, debinding and sintering components [4-6]. The goal of mixing steps is to form the feedstock for hot embossing by mixing the metallic powders with thermoplastic binders. The binders used in hot embossing are commonly used polymer mixtures, such as polypropylene, a synthetic or natural wax and stearic acid. The resulting mixture is called a feedstock, which is then embossed in a mould to achieve the required shapes. Afterwards, the binder is removed during thermal debinding, and the powder is sintered, yielding the full density necessary to

give the required mechanical properties and geometric size; at the same time, a certain amount of shrinkage occurs (see Fig. 1).

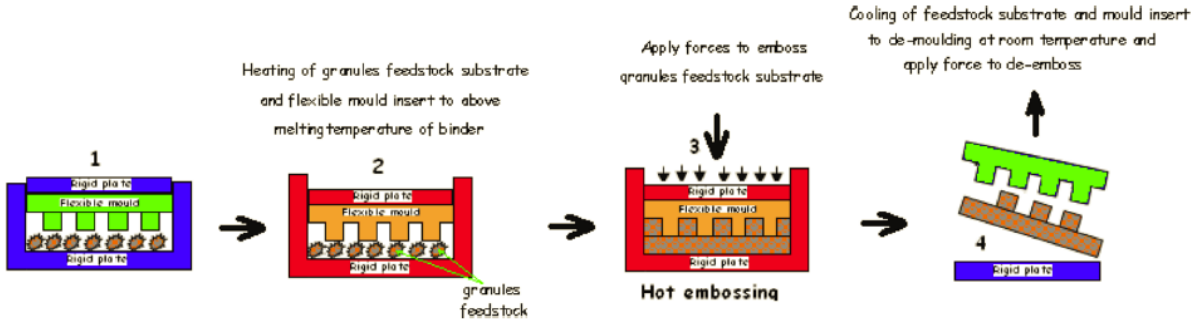

Figure 1: Illustration of the hot embossing process to create micro-devices.

In the MHE process, the metallic components undergo contraction and deformation, leading to challenges in terms of determining the initial structure design of the die mould cavities, the initial size and the processing parameters. Traditionally, in this stage, trials and error methods or empirical formulas have always been applied to control the part shape and dimensional accuracy; however, this has resulted in a high experimental cost and limited control precision. For these reasons,, performing a finite element simulation can be an effective alternative to predict part deformation and estimate anisotropic shrinkages in micro-structured components arising from the MHE process. The first sintering model was developed at the grain scale with only one diffusion mechanism [7]. Then, models improved by coupling several mechanisms and by modifying the geometry of the systems. In addition, the problem can also be solved analytically for simple geometries with a thermo-elastic model [8]. Then, finite element analysis (FEA) is can be used as an effective tool when considering samples with complex geometries and complex boundary conditions [9], or to account for other phenomena such as gravitational effects or a thermal gradient, which induce constrained sintering [10]. The objective of the present work is to predict of anisotropic shrinkages and estimated the dimensional changes of micro-structured components during the sintering step with the FE method. The goal of these simulations is to also provide information regarding the evolution of density variations. In this paper, the material and process sintering parameters are identified from dilatometer experimental datas. The model and the identified material parameters are implemented in a finite element solver to perform the numerical simulation of the sintering step associated to with MHE. Sintering experiments were performed in a batch furnace to verify the numerical model and simulations on 316L stainless steel.

2 CONSTITUTIVE EQUATIONS FOR THE SINTERING PROCESS

Compared with conventional trial and error methods, numerical simulations of sintering using finite element methods can be more effective by minimizing the effects of tooling and processing parameters [11]. The proposed model is based on the assumption that a porous material follows a linear-viscous behavior and behaves according to the continuum theory of sintering [12]. This model is a phenomenological model based on continuum mechanics and uses thermo-elasto-visco-plastic formulations, which are related by the following eq. [13]:

$$\dot{\varepsilon} = \dot{\varepsilon}_e + \dot{\varepsilon}_{th} + \dot{\varepsilon}_{vp} \Rightarrow \dot{\varepsilon} = C_e \dot{\sigma} + \alpha \Delta \dot{T} I + \frac{dev\sigma}{2G_p} + \frac{\sigma_m - \sigma_s}{3K_p} I \quad (1)$$

where εe, εth and εvp are the elastic, thermal and viscoplastic strains rates, respectively, Ce is the elastic compliance matrix, ΔT is the incremental temperature rate, I is the second order identify tensor, α is the thermal expansion coefficient was determined experimentally using a dilatometer, σm = tr(σ)/3 is the trace of the stress tensor, G and K are the shear and bulk viscosity moduli, respectively, and σs is the sintering stress. The variables G, K and σs are material parameters that still need to be determined. The elastic-viscous analogy is used to define the shear and bulk viscosity moduli for sintering materials [14]:

$$G_p = \frac{\eta_p}{2(1+\nu_p)}; \; K_p = \frac{\eta_p}{3(1-2\nu_p)} \quad (2)$$

where ηp and νp are the uniaxial viscosity and viscous Poisson's ratio of a porous material, respectively. Song et al. (2006) derived the following relationship to define the uniaxial viscosity ηp through bending tests in a dilatometer [15]:

$$\eta_p = \frac{1}{\dot{\delta}}\left(\frac{5\rho_0 g L_s^4}{32h^2} + \frac{PL_s^3}{4bh^3}\right) \quad (3)$$

where δ is the deflection rate at the centre of the specimen, ρa is the apparent density, g is gravity, P is the external load, and L_s, b and h are the distance between the two supporting rods and the width and thickness of the specimen [16]. Bordia [16] and Scherer [17] related a phenomenological expression to calculate Poisson's ratio of the sintered material as follows:

$$\nu_p \approx \sqrt{\frac{\rho}{3-2\rho}}; \; \rho = \frac{\rho_0}{(1+\lambda)^3} \quad (4)$$

where ρ is the relative density and λ is the uniaxial shrinkage, which is defined as:

$$\lambda = \frac{L - L_0}{L_0} \quad (5)$$

where L_0 and L are the length of the specimens before and after sintering, respectively. The following equation is used to determine the sintering stress [18]:

$$\sigma_s = Bd^c \quad (6)$$

where B and C are material parameters identified from dilatometry experiments.

Using these proposed constitutive equations, the related material parameters can be determined. The identification algorithm was designed to properly identify of the material parameters B and C used in the sintering stress model to optimise the numerical simulations. The following equation was proposed to calculate the stress during the sintering stage [18]:

$$\frac{\mathrm{dL}}{\mathrm{Ldt}} = \alpha \dot{T} - \frac{\sigma_s}{3K} \quad (7)$$

The proper strategy consists of identifying parameters B and C which determine the numerical shrinkage curve according to Eq. (8), in Matlab®. Therefore, the minimisation algorithm is used to, as best as possible, fit the simulations to the experimental curves by adjusting the physical parameters [18]:

$$\begin{cases} \min G(x) \\ G(x) = \sum_{i=1}^{n} \left| \lambda^{\exp}(T_i, x) - \lambda^{num}(T_i, x) \right|^2 \\ x = [B, C] \end{cases} \quad (8)$$

where λe is the experimental uniaxial shrinkage obtained from the dilatometry tests, λm is the numerical uniaxial shrinkage, F(x) is the mean residual squares of the tolerance, with i = 1,…, n indicating the different sintering temperatures, and x is the set of material parameters that need to be identified.

3 MATERIALS AND EXPERIMENTAL METHODS

3.1 Materials

The powders used to develop the feedstock dedicated to the MHE process are fine 316L stainless steel powders that exhibit excellent mechanical and corrosion properties, as well as biocompatibility. In the present analysis, the stainless steel powders (Osprey® Sandvik, UK) used exhibits a particle size distribution as follows: d10=1.8 µm, d50=3.5 µm and d90=5.0 µm (see Fig. 2a).

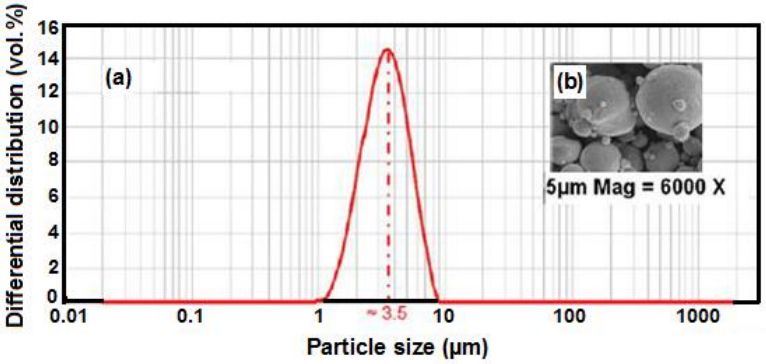

Figure 2: (a) Particle size distribution and (b) SEM micrograph of the 316L stainless steel powder.

Table 1: Characteristics of the 316L stainless steel powders.

Powder size and density						
Powder	Particle shape	D_{10} (µm)	D_{50} (µm)	D_{90} (µm)	Density [g/cm^3]	Tap density [g/cm^3]
Inox 316L	Spherical	1.8	3.4	5.0	7.90	4.50

The binder system used in this study consisted of paraffin wax (PW), polypropylene (PP) and stearic acid (SA), and the highest melting temperature of the binder system measured on a Setaram differential scanning calorimeter (DSC 92) is 160 °C. The composition of the binder, which corresponds to the ratio of PP/PW/SA, is given as the relative fractions 40/55/5. The characteristics of the different binder systems and the raw powders are presented in Tables 1 and 2. Experiments related to the mixing of binders and feedstocks were performed using a twin-screw Brabender® Plastograph EC mixer with a pair of rotor blades. The same

processing conditions were used for each mixture, including a mixing temperature of 180 °C, a mixing time of 30 min and a mixing rotation speed of 30 rpm.

Table 2: Characteristics of the different binder components.

Binders	Density [g/cm^3]	Melting temperature [°C]
Stearic acid (SA)	0.89	70
Paraffin wax (PW)	0.91	60
Polypropylene (PP)	0.90	160

4 FINITE ELEMENT MODELLING OF THE SINTERING PROCESS

4.1 Boundary and initial conditions

A micro-fluidic geometry with the dimension of 70x30x5 mm^3 with and micrometric grounds on the order of 100 µm, is shown in Fig. 3a. The element type and mesh are defined for the geometries as shown in Fig. 3b. We have used anisotropic meshes with the correct mesh concentration that consist of a fine mesh for the micro-fluidic patterns and a coarse mesh for the body of the piece. The anisotropic mesh of micro-fluidic component is composed of 141874 nodes and 92328 C3D8R elements and the densification support used is composed of 1896 nodes and 1170 R3D4 elements. The plate support is assumed to be a rigid body during the simulation, and the micro-fluidic replicas follow thermo-elasto-viscoplastic behaviour.

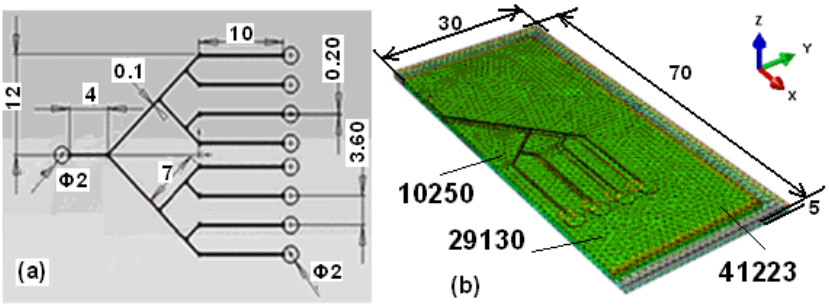

Figure 3: (a) Geometry of micro-fluidic specimens. Dimensions of samples under sintered condition, (b) FE meshes of the micro-fluidic component and the plate support prior to the simultaneous sintering stages.

Based on previous studies, different densification kinetics were retained and corresponds to heating rates of 5 °C/min, 10 °C/min and 15 °C/min to a maximum sintering temperature of 1360 °C. In addition, the «Pressure/Over-closure» contact was selected for the components. For free sintering, Coulomb's frictional law was also used in the simulation [19]. The experiments to determine the frictional coefficient have not yet been performed. However, several values, which range from 0.1 to 0.8, were chosen as the friction coefficient in the numerical simulations. The results of the simulation with the friction coefficient equal to 0.5 are the closes to the experimental results. The density distributions obtained in the hot embossing stage are regarded as the initial conditions of the sintering process with inhomogeneous green density conditions.

Table 4: Changes in the relative density due to sintering at three nodes in the FEM model of the micro-fluidic specimen (see Fig. 6).

Node number	Initial relative density	Final relative density
10250	0.612	0.969
29130	0.618	0.975
41223	0.624	0.976

4.2 Numerical results and discussion

In the powder hot embossing process, segregation occurs between the powders and binders due to their different values of inertia. This induces inhomogeneous density distributions in the green parts. This initial in-homogeneity affects the final dimensions and mechanical properties of the sintered components. The initial and final distribution of relative density after the embossing and sintering stages, respectively obtained by simulation, have been shown in Figure 4. Fig. 4a displays the relative density distribution contour after hot embossing, with its lowest value of 61.20% in the central area and highest value of 62.4% at the outside of the micro-fluidic component. The relative density gap was broadened by ~2% during the hot embossing process, and narrowed after sintering. This finding is observed primarily due to the considerable compression effects of the rubber mould cavities as well as the non-homogeneous loading conditions in terms of the complicated structure.

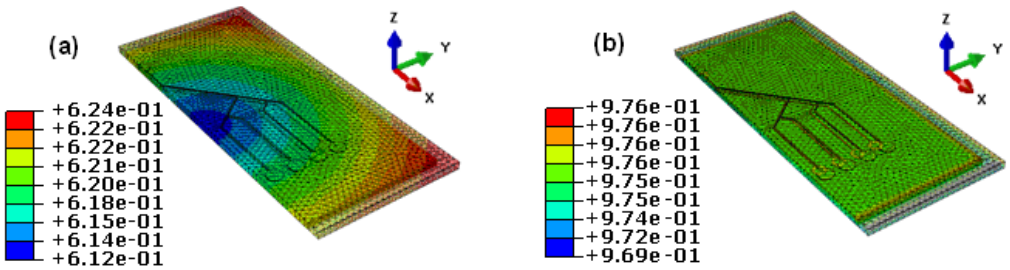

Fig. 4. Final distribution of the relative density in micro-fluidic specimens of 316L stainless steel powders, obtained after the (a) hot embossing process and (b) sintering stage at 1360 °C (solid loading: 60%, heating rate: 15 °C/min, hold time: 120 min).

The influence of the heating rates on the density of the sintered parts is shown in Fig. 5. After the sintering stage, the relative densities are generally homogeneous for most of the simulations, in which the variations have been well controlled within 2%. In addition, the numerical data clearly indicate that the sintering temperature has a significant effect on the sintered density. It was also found that the heating rate only has a significant effect on the sintered density at 1250 °C, which increase the average sintered density from 7.11 g/cm^3 to 7.27 g/cm^3. It can be observed that the final density distribution is still essentially uniform and more homogeneous when the heating rate is equal to 15 °C/min. Generally, all of the sintering variables have a significant effect on the sintered density. The numerical data show that the sintering temperature has the highest influence on the sintered density (64%), followed by the

heating rate (8%), solid loading (4%) and two-factor and three-factor interactions. Other sintering variables, not taken into account in our simulations, also have a significant effect on the sintered density such as the sintering atmosphere and sintering time.

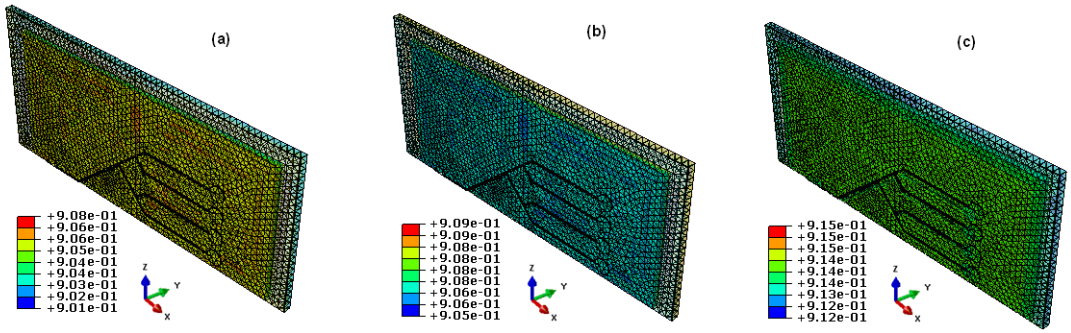

Figure 5: Final relative density of the sintered micro-fluidic components after sintering at 1250°C with a heating rate equal to: (a) 5°C/min, (b) 10°C/min and (c) 15°C/min (solid loading: 60%, hold time: 120 min).

In addition to the relative densities, the shrinkages were also simulated for these micro-fluidic components embossed with different conditions. The heating rate is one of the most important process parameters of sintering processes. It has been observed that the maximum shrinkage rate depends on the heating rates; however, the peaks of the maximum shrinkage rate located in a narrow temperature range. In fact, this narrow range spans merely from 1250 °C to 1360 °C. It is obvious that rapid sintering is favourable for densification; however, fast sintering can induce a crack in the sintered body due to the high thermal or stress gradients. In addition, the final shrinkage decreases with increasing solid loading (see Fig. 6). It can be clearly observed that the shrinkage value was stable and homogeneous, due to the symmetrical geometry. In addition, the shrinkage values increases with increasing heating rate, where it was observed that the shrinkage value was more stable and homogeneous at 15 °C/min.

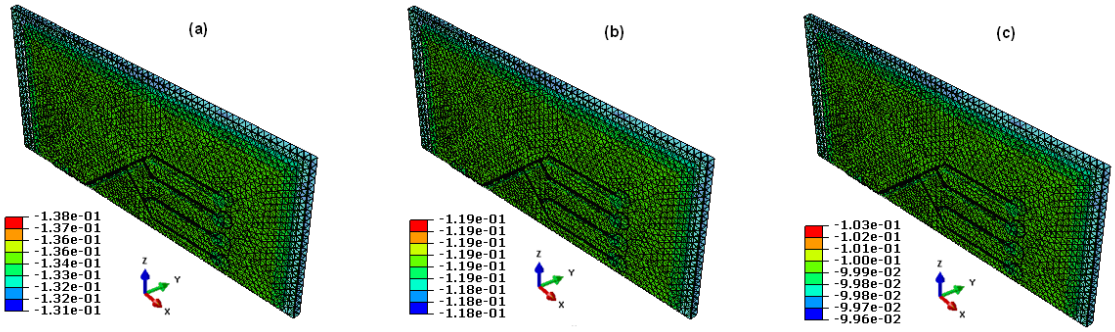

Figure 6: Numerical final shrinkage of the sintered micro-fluidic components after sintering at 1360°C using different solid loading conditions of (a) 60%, (b) 62% and (c) 64% (heating rate: 15°C/min, hold time: 120min).

5 EXPERIMENTAL RESULTS AND DISCUSSION

The microfluidic samples with the PP-based binder have been obtained using hot embossing process, then were subjected to thermal debinding at 500 °C for 1 h and were

subsequently sintered in a high-vacuum furnace at 1360 °C for 2 h. The sintered samples were free of physical defects (see Fig. 7).

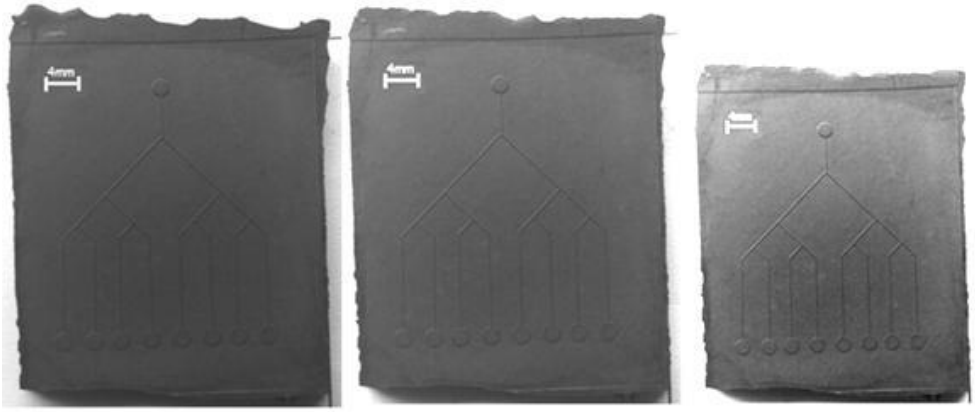

Figure 7: Photographs of the micro-fluidic replicas after the: (a) embossing (b) debinding and (c) sintering steps, which were produced using 316L stainless steel feedstock (with a solid loading of 64%).

The shrinkage values were measured using an Alicona Infinite Focus confocal microscope at twenty chosen points, as shown in Fig. 8. The dimensional changes in the length and width of the micro-structures show similar trends. The shrinkage in the thickness direction is greater than that in the other directions. This same phenomenon has been encountered by other researchers, such as Loh et al. (1996).

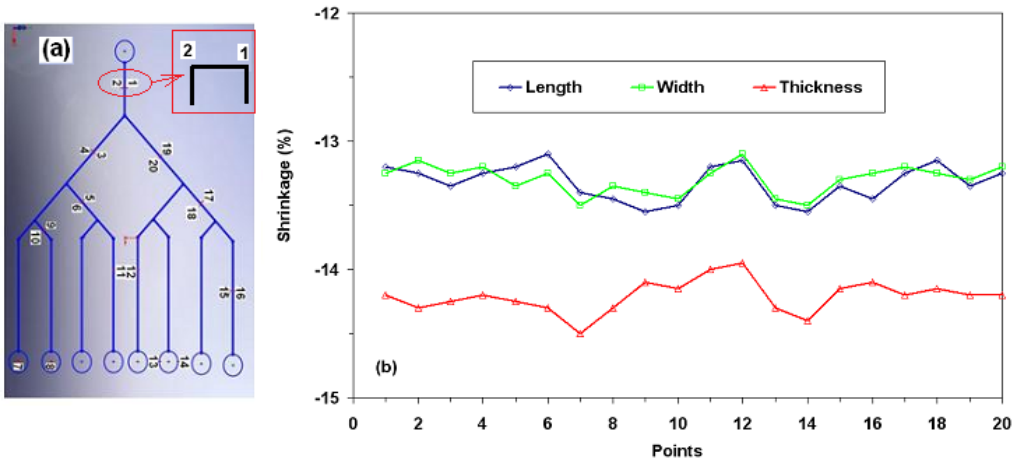

Figure 8: (a) Positions of twenty points chosen to measure the shrinkages of the sintered part (b) shrinkages of the sintered part in different directions, which was measured by an Alicona microscope at the twenty chosen points (solid loading: 60%, heating rate: 15°C/min, sintering temperature: 1360°C).

The dimensions of the micro-fluidic samples are given in Table 5. The relative densities were also determined by the Archimedes water immersion method, and porosity was evaluated using an image analyser device. The theoretical density of stainless steel powder is 7.90 g.cm^{-3}. The sintering temperature had a significant effect on the densification, i.e., the density increased significantly with increasing temperature, as summarized in Fig. 9. The

influence of sintering temperature on the densification of 316L stainless steel is more pronounced; a significant densification was observed when the stainless steel tool became mushy at 1300 °C. The maximum density was obtained when sintering was performed at 1360 °C, which was 98.2% of the theoretical values. The heating rate also has a strong effect on the final density. The porosity is lower and the grains become finer as the heating rate increases.

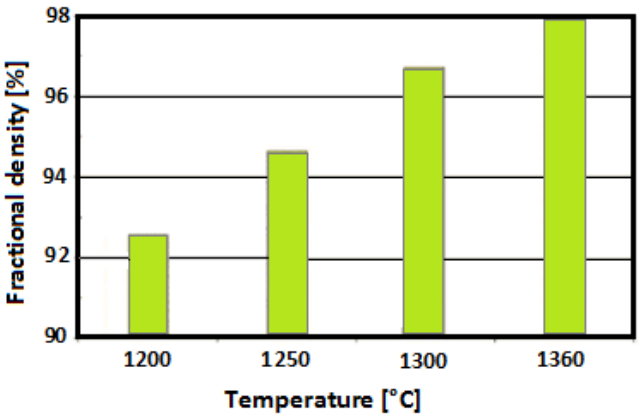

Figure 9: Effect of sintering temperature on the sintered density (dwell time 120min, 15°C/min).

Table 5: Dimensions of the elastomeric mould and micro-sized structures of the micro-fluidic samples.

Micro-sized structure / 316L stainless steel 1360°C - 15°C/min				
		60%	62%	64%
Φ	2	1.72±0.01	1.76±0.01	1.78±0.01
a	5	4.31±0.01	4.41±0.01	4.49±0.01
b	14	12.11±0.01	12.40±0.01	12.53±0.01
c	14	12.15±0.01	12.33±0.01	12.54±0.01
d	4	3.45±0.01	3.53±0.01	3.56±0.01
e	14	12.16±0.01	12.39±0.01	12.55±0.01

6 EXPERIMENTAL VALIDATION

The relative density of the micro-fluidic specimens obtained from the numerical simulations is compared with the experimental values, as shown in Fig. 10. The relative densities are in perfect agreement with the experimental densities, particularly for the sintering cycles with relatively low heating rates. A comparison between the experimental and the simulation results of the shrinkage in three directions (length, width and height) is also shown in Fig. 11. During the sintering stage, the simulated dimensions were in good agreement with the experimental values, with a relative error of less than 3% in both directions. In addition, both the simulated and experimental shrinkages in the height direction were higher than those in the other two directions, which is primarily due to gravity along the height direction. During the sintering process, the relative errors between the simulated and experimental results in the height direction were found to be greater than 5%. This result is

primarily due to the structural anisotropy of the parts processed. This same phenomenon has been encountered by other researchers, such as Loh et al. (1996).

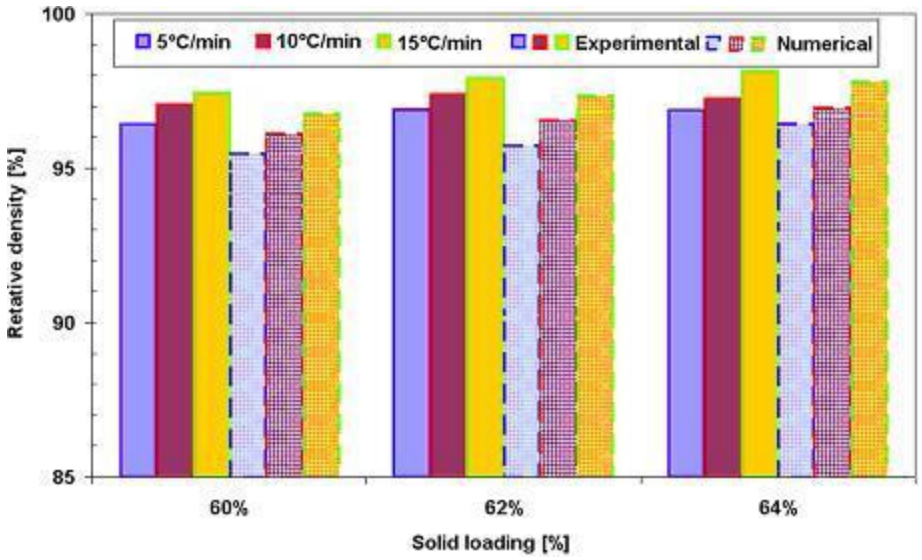

Figure 20: Comparison between the experimental and simulated results of the relative density.

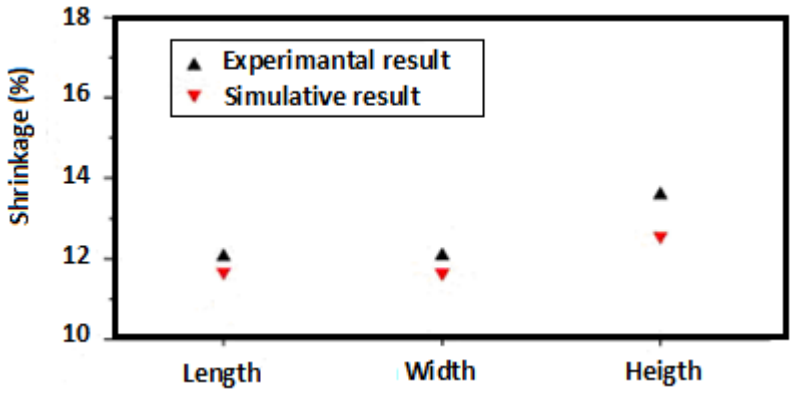

Figure 31: Comparison between the experimental and simulated results of shrinkage in three directions.

7 CONCLUSIONS

A numerical simulation based on a finite element analysis was performed in order to investigate the shrinkage variations and relative density evolutions during a powder hot embossing process. The simulation results are in good agreement with the experimental data, which proves the validity of the physical model and the reliability of the identification and numerical method. The following conclusions can be made:

- The sintering experiments using a dilatometer demonstrate that the sintering parts in 316L stainless steel have the threshold temperatures in the range of 1050 to 1080 °C. In

addition, the rapid sintering is favourable for densification. The maximum shrinkage of 316L stainless steel powders is 14%, at a heating rate of 15 °C/min.

- It can also be observed that the sintering process makes the final density of the sintered bodies essentially uniform, whereas in-homogeneity of the initial density primarily affects uneven shrinkage of the sintered body. In fact, the micro-fluidic components exhibit very small shrinkage after the hot embossing and debinding stages. However, the components exhibit inhomogeneous shrinkage after sintering, which ranges from 11.5% to 14%.

REFERENCES

[1] Santos P. F., Niinomi M., Liu H., Cho K., Nakai M., Itoh Y., Narushima T., Ikeda M., Fabrication of low-cost beta-type Ti–Mn alloys for biomedical applications by metal injection molding process and their mechanical properties, *Journal of the Mechanical Behavior of Biomedical Materials*(2016)**59**:497-507.

[2] Ou H., Sahli M., Gelin J.-C., Barrière T., Experimental analysis and finite element simulation of the co-sintering of bi-material components, *Powder Technology*(2014)**268**:269-278.

[3] Zhao D., Chang K., Ebel T., Qian M., Willumeit R., Yan M., Pyczak F., Microstructure and mechanical behavior of metal injection molded Ti–Nb binary alloys as biomedical material, *Journal of the Mechanical Behavior of Biomedical Materials*(2013)**28**:171-182.

[4] Sahli M., Gelin J.-C., Barriere T., Characterisation and replication of metallic microfluidic devices using three different powders processed by hot embossing, *Powder Technology*(2013)**246**:284-302.

[5] Kurgan N., Effects of sintering atmosphere on microstructure and mechanical property of sintered powder metallurgy stainless steel, *Materials & Design*(2013)**52**:995-998.

[6] Sahli M., Gelin J.-C., Barrière T., Replication of microchannel structures in WC–Co feedstock using elastomeric replica moulds by hot embossing process, *Materials Science and Engineering: C*(2015)**55**:252-266.

[7] Coble R. L., Sintering crystalline solids. I. Intermediate and final state diffusion models, *J. Appl. Phys* (1961)**32**:787-792.

[8] Wakai F., Mechanics of viscous sintering on the micro- and macro-scale, *Acta Mater*(2013)**61**:239-247.

[9] Reiterer M., Kraft T., Janosovits U., Riedel H., Finite element simulation of cold Isostatic pressing and sintering of SiC components. Ceram Int (2004)**30**:177-183.

[10] Bruchon J., Pino-Munoz D., Valdivieso F., Drapier S., Finite element simulation of mass transport during sintering of a granular packing. Part I. Surface and lattice diffusions, *J. American Ceramic Society*(2010)**13**:1-23.

[11] Yu P.C., Li Q.F., Fuh J.Y.H., Li T., Lu L., Two-stage sintering of nano-sized yttria stabilized zirconia process by powder injection moulding, *J. Mater. Process. Technol*(2007)**192**:312-318.

[12] Olevsky E.A., Theory of sintering: from discrete to continuum, *Mater. Sci. Eng*(1998)**23**:41-100.

[13] Gasik M., Zhang B., A constitutive model and FE simulation for the sintering process of powder compacts, *Comput. Mater. Sci*(2000)**18**:93-101.
[14] Bouvard D., McMeeking R.M., Deformation of interparticle necks by diffusion controlled creep. *J. Am. Ceram. Soc*(1996)**79**:666-672.
[15] Song J., Gelin J.C., Barrière T., Liu B., Experiments and numerical modelling of solid state sintering for 316L stainless steel components, *Journal of Materials Processing Technology*(2006)**177**:352-355.
[16] Bordia R.K., Scherer G.W., On constrained sintering. I. Constitutive model for a sintering body, *Acta Mater*(1988)**36**:2393-2397.
[17] Scherer G.W., Sintering inhomogeneous glasses: application to optical waveguides, *J. Non-Cryst. Solids*(1979)**34**:239-256.
[18] Peterson A., Agren J., Constitutive benhavior of WC–Co materials with different grain size sintered under load, *Acta Mater* (2004)**52**:1847-1858.
[19] Olevsky E. A., German R. M., Upadhyaya A., Effect of gravity on dimensional change during sintering- Π shape distortion, *Acta Mater*(2000)**48**:1167-1180.
[20] Loh NH, German RM, Statistical analysis of shrinkage variation for powder injection molding. *J Mater Process Technol*(1996)**59**:278-284.